Results in Engineering 17 (2023) 100895

Contents lists available at ScienceDirect

Results in Engineering

journal homepage: www.sciencedirect.com/journal/results-in-engineering

Experimental and computational studies on the formation of mixed amide-hydride solid solutions for $CsNH_2$–CsH system

Thi-Thu Le [a,**], Archa Santhosh [a], Simone Bordignon [b], Michele R. Chierotti [b], Paul Jerabek [a], Thomas Klassen [a,c], Claudio Pistidda [a,*]

[a] Institute of Hydrogen Technology, Helmholtz-Zentrum Hereon GmbH, Max-Planck-Straße 1, D-21502, Geesthacht, Germany
[b] Department of Chemistry - University of Torino, V. P. Giuria 7, I-10125, Torino, Italy
[c] Helmut Schmidt University, Holstenhofweg 85, 22043, Hamburg, Germany

ARTICLE INFO

Keywords:
Amide-hydride solid solution
Density functional theory
Spectra simulation
Anionic substitution

ABSTRACT

In this study, experimental determination and computational prediction are combined to investigate the formation of a mixed amide-hydride solid solution for the $CsNH_2$–CsH system in a wide compositional range. The experimentally obtained results strongly indicate that a complete amide-hydride solid solution $Cs(NH_2)_xH_{1-x}$ with a stable cubic structure is achievable when the molar fraction of amide (x) is lower than 0.9. These results validate and confirm our data computationally via first-principles calculations, including the simulations of infrared (IR) and nuclear magnetic resonance (NMR) spectra for structures of various compositions as well as the determination of the dipolar coupling constants. Both the computed vibrational frequencies and ^{1}H chemical shifts of $CsNH_2$ and CsH moieties in the $Cs(NH_2)_xH_{1-x}$ (x = 0.2, 0.5, 0.8, 1) solid solution structures agree with the experimental IR and ^{1}H MAS NMR data of the mixed $xCsNH_2$+(1-x)CsH samples, confirming the formation of the solid solutions. The closest interproton distance in the homogeneous $Cs(NH_2)_{0.5}H_{0.5}$ solid solution is computed to be 3.67 Å, which is larger than that of the known $Rb(NH_2)_{0.5}H_{0.5}$ solid solution (3.29 Å). This work's combination of theoretical research and experimentation provides a suitable framework for the structural analysis and property estimation of other M-N-H solid solutions.

1. Introduction

In the field of hydrogen research, amide-hydride solid-state materials are known as promising candidates to store hydrogen effectively and safely. In 2002, Cheng et al. [1] discovered the possibility of reversible hydrogen storage in lithium amide-hydride systems, e.g., $LiNH_2$–LiH. Since then, metal amide-hydride mixtures such as systems based on Mg$(NH_2)_2$–2LiH [2–9], KNH_2–MgH_2 [10], KH–Mg$(NH_2)_2$ [10], Mg$(NH_2)_2$–RbH [11], and $LiNH_2$–LiH [12–16], have been extensively investigated as potential hydrogen storage materials for mobile and stationary applications due to their high hydrogen storage capacity and favorable thermodynamics, which in many cases allow for the reversible release of hydrogen at temperatures below 150 °C. However, amide-hydride systems are currently limited to practical applications due to their sluggish dehydrogenation/re-hydrogenation kinetics [4–6, 17–19]. In this context, a deeper understanding of the existing kinetic limitations is crucial for the development of advanced amide-based materials. In amide-hydride systems, the interplay between H^+ ions of the amide phases and the H^- ions of the hydride phases promotes the formation of intermediate phases. Numerous attempts have been made to improve the hydrogen sorption rates of metal amide-hydride systems, either by using targeted additives [8,20–28], or via the particle size reduction of the material [29–32]. Ionic hydrides, such as KH, RbH, and CsH, were found to lower the operating temperature of the system and improve the hydrogen sorption rates of the Li–Mg–N–H system [10,20, 33–38]. These improvements are ascribed to the formation of intermediates ($MMgNH_2NH$) resulting from the interaction between Mg$(NH_2)_2$ and MH (M = K, Rb, Cs) [10,11,34,35]. In addition, it was also reported that the crystallographic structure of the intermediates $KMgNH_2NH$ and $RbMgNH_2NH$ in the K–Mg–N–H and the Rb–Mg–N–H systems, respectively are similar [10,11]. These intermediate phases lower the kinetic barrier of the interfacial reaction between Mg$(NH_2)_2$ and KH, and/or RbH in the KH- and/or RbH-doped Mg$(NH_2)_2$– 2LiH system. In contrast, for other alkali amide-hydride systems, it was also

* Corresponding author.
** Corresponding author.
E-mail addresses: thi.le@hereon.de (T.-T. Le), claudio.pistidda@hereon.de (C. Pistidda).

https://doi.org/10.1016/j.rineng.2023.100895
Received 16 November 2022; Received in revised form 3 January 2023; Accepted 13 January 2023
Available online 14 January 2023

demonstrated that the extent of amide-hydride or amide-imide incorporation leads to a mixed metal amide/imide-hydride solid solution. This formation of amide/imide-hydride solid solution is mostly due to the partial substitution of anionic species which is well-known as an effective approach to enhance the ionic conduction of a material [39,40]. The formation of a homogeneous solid solution leads to modified structures of the material, resulting in the improvement of the ionic conductivity of the host materials [41–43]. Several alkali amide-hydride solid solutions have been published so far, for example, $Li_{2-x}NH_{1+x}$ solid solutions were independently reported by Makepeace et al. and David et al. [16,44,45]. Santoru et al. [11,46] have also observed the formation of the solid solutions $K(NH_2)_xH_{1-x}$ and $Rb(NH_2)_xH_{1-x}$ in KNH_2–KH and $RbNH_2$–RbH systems, respectively. The authors claimed that $K(NH_2)_xH_{1-x}$ and $Rb(NH_2)_xH_{1-x}$ solid solutions are formed by the exchange of amide/hydride anions at the amide/hydride interface and the structural properties of these two solid solutions, i.e. $K(NH_2)_xH_{1-x}$ and $Rb(NH_2)_xH_{1-x}$, are analogous.

Given the chemical similarities of potassium, rubidium, and cesium compounds [47,48] and the similar performance of KH, RbH, and CsH as additives that can improve the hydrogen storage properties of the Li–Mg–N–H system [38,49], the probability of the formation of a $CsNH_2$–CsH solid solution is high.

In the frame of this work, we have carried out a systematic study on the $CsNH_2$–CsH system as a function of the $CsNH_2$/CsH ratio by combining experimental evidence (e.g. *ex-situ* and *in-situ* XRD, IR, NMR) and theoretical calculations (e.g. first-principles calculations for structures of solid solution, IR/NMR spectra simulations), the focus being on investigating the formation of Cs–N–H solid solutions. The obtained results are described and discussed in the following sections. With this study, we aim to create an accessible library of Cs–N–H materials that can be further investigated for their functional properties as catalysts, additives, or ionic conductors as well as to provide a reliable method with controlled stoichiometry for synthesizing other functional M-N-H solid solutions.

2. Experimental method

2.1. Sample preparation

Cesium hydride (CsH) was synthesized by ball-milling metallic cesium (Alfa Aesar, 99.8%) in 50 bar of hydrogen (H_2) at 500 rpm for 13 h, using a ball-to-powder ratio (BPR) of 60:1. To obtain CsH powder as a final product, the milled material was subsequently annealed at 160 °C under 70 bar of H_2 for 3 h. Cesium amide ($CsNH_2$) was prepared by ball-milling the synthesized CsH at 500 rpm with a BPR of 20:1 under an ammonia (NH_3) atmosphere of 7 bar. The overall milling time was 4 h, divided into 2 cycles of 2 h milling and a pause of 30 min in between. This was repeated four times reaching an overall milling time of 16 h. Between each repetition, the milling vial was evacuated and refilled with fresh NH_3. To avoid detrimental atmospheric contaminations, all samples were prepared in an argon-filled glovebox (MBraun, Germany) with oxygen and moisture concentration ≤1 ppm. Mixtures of $CsNH_2$ and CsH were prepared at different stoichiometric ratios according to the following reaction:

$$CsNH_2 + (1+x)CsH \rightarrow Cs(NH_2)_xH_{(1-x)} \quad (1)$$

where x is the molar fraction of $CsNH_2$, and x = {0, 0.1, 0.2, 0.3, 0.5, 0.7, 0.8, 0.9, 1}. The material mixtures were prepared by hand-grinding using an agate mortar. The annealing process was carried out by heating the materials from room temperature (RT) to 140 °C and keeping them at 140 °C for 3 h. For the ball-milled samples, the material mixtures were milled in an 8000 M Mixer/Mill® High-Energy Ball Mill (SPEX SamplePrep LLC, Metuchen, NJ, USA) for 10 min using a stainless steel vial and stainless steel balls with a BPR of 10:1.

2.2. Material characterization

Ex-situ powder X-ray diffraction (XRD) experiments were performed using a D8 Discover diffractometer (Bruker AXS GmbH, Karlsruhe, Germany) equipped with a Cu Kα radiation (λ = 1.54184 Å) and 2D VANTEC detector. The diffractograms were acquired in the 2θ range from 10° to 90°, in nine steps with an exposure time of 300 s per step. In an argon (Ar)-filled glovebox (oxygen and moisture concentration ≤1 ppm), a small amount of sample was placed onto a flat commercial sample holder and sealed with an airtight lid made of poly(methylmethacrylate) which is used to prevent air contamination of the sample.

In-situ Synchrotron Powder X-ray diffraction (*in-situ* SR-PXD) experiments were carried out at the diffraction beamline (P02.1) of Petra III (Desy Hamburg, Germany) [50] using a monochromatic X-ray beam (λ = 0.20761 Å). The diffracted patterns were collected by a PerkinElmer XRD 1621 2D detector with an array of 2048 × 2048 pixels and a pixel size of 200 μm × 200 μm, using an exposure time of 10 s per scan. The samples were loaded under a purified argon atmosphere in sapphire capillaries and then mounted on an *in-house* developed *in-situ* cell, in which operating temperatures and pressures can be controlled [51,52]. All measurements were carried out under 1 bar of Ar, the sample was heated up from RT to 140 °C with a heating rate of 5 °C·min^{-1}, kept isothermally at 140 °C for 10 min, and after that cooled to RT. The 2D diffraction images were integrated into 1D diffractograms *via* the FIT2D software and the quantitative analyses were performed by the Rietveld refinement method using the MAUD software (Material Analysis Using Diffraction) [53]. Structural information of known phases was obtained from the Inorganic Crystal Structure Database (ICSD) *via* the software ICSD-Desktop.

The pristine and mixture samples were characterized by the FT-IR technique (Cary 630 FT-IR spectrometer, Agilent Technologies Deutschland GmbH, Waldbronn, Germany). The FT-IR spectrometer was placed inside an argon circulation glovebox with concentrations of oxygen and moisture lower than 5 ppm. The background was calibrated for each measurement. For each measurement, a small amount of material was placed on the diamond ATR top plate, and the FT-IR spectrum was acquired at RT in a full frequency range of 4000–650 cm^{-1} with a spectral resolution of 4 cm^{-1} and a number of scans of 300.

Differential thermal analysis (DTA) investigations were carried out using a Netzsch STA 409 calorimeter. The sample (~20 mg) was heated from RT to 140 °C with a heating rate of 5 °C·min^{-1}, under an argon flow of 50 mL min^{-1}.

Solid-state NMR experiments were run on a Bruker AVANCE II 400 instrument operating at 400.23 MHz for ^{1}H and equipped with a 2.5 mm probe. Rotors were packed inside a glovebox to prevent sample decomposition. The ^{1}H MAS spectra were acquired at the spinning speed of 32 kHz with the DEPTH sequence (π/2–π–π) for the suppression of the probe background signal (^{1}H 90° = 2.5 μs; 16 scans; relaxation delay equal to 131.5 s, corresponding to 5·T_1). 2D ^{1}H double-quantum (DQ) MAS experiments were performed at 32 kHz using the back-to-back (BABA) recoupling pulse sequence with excitation time equal to the period of the rotor (^{1}H 90° = 2.5 μs; 32 scans; t_1 increments = 46; relaxation delays equal 33.4 s, corresponding to 1.27·T_1). ^{1}H scale was calibrated with adamantane (^{1}H signal at 1.87 ppm with respect to TMS - tetramethylsilane) as external standard.

2.3. Computational methodology

The experimental findings on the formation of the amide-hydride solid solution were evaluated with first-principles calculations. Guess structures for the $Cs(NH_2)_xH_{(1-x)}$ with x = {0.2, 0.5, 0.8} were generated with the structure transformation module implemented in the Python Materials Genomics (pymatgen) library [54]. The selection of the structures for this study took into account the different orientations of the amide and hydride moieties, the lattice parameters obtained from the Rietveld refinement of XRD patterns, and the calculated total

energies. Accordingly, the best appropriate structural models for Cs$(NH_2)_xH_{1-x}$ with x = {0.2, 0.5, 0.8} is illustrated in ESI-Fig. S1.

Density functional theory (DFT) calculations of the structural and vibrational properties were performed with the Vienna *ab initio* simulation package (VASP) version 5.4.4 [55,56] using the projected augmented-wave (PAW) method [57,58]. The exchange and correlation effects were described within the generalized gradient approximation (GGA) of the Perdew-Burke-Ernzerhof functional for solids and surfaces (PBEsol) [59]. All structural relaxations were carried out with an energy and force convergence criteria of at least 10^{-5} eV/unit and 10^{-2} eV/atom, respectively, with a tested plane-wave kinetic energy cut-off of 480 eV. A *k*-point sampling grid corresponding to a *k*-spacing of 0.4 $Å^{-1}$ was used. Only the ionic positions were allowed to fully relax and the long-range dispersive interactions were taken into account by using the DFT-D3 dispersion correction with Becke-Johnson damping [60,61].

Simulated IR spectra: The force constant matrices required to determine the phonon frequencies of the optimized Cs$(NH_2)_xH_{1-x}$ with x = {0.2, 0.5, 0.8, 1} structures were computed with density functional perturbation theory (DFPT) [62,63] in the harmonic approximation. The Phonopy package version 2.10.0 [64] in combination with Phonopy-Spectroscopy [65] was then used to simulate the IR spectra.

Simulated NMR spectra: NMR parameters were calculated with the gauge-including projector-augmented wave (GIPAW) [66] approach implemented in the Cambridge serial total energy package (CASTEP) [67] version 20.11. "On-the-fly" generated ultrasoft pseudopotentials [68] necessary for the NMR calculations were also employed for the prior structural relaxations with CASTEP with a plane-wave energy cut-off of 840 eV. Relativistic effects were included with the zeroth-order regular approximation (ZORA) [69] to the Dirac equation. The charge-density dependent Tkatchenko-Scheffler (TS) [70] correction was applied to include dispersion effects taking into account the local chemical environment of the atoms. The reference chemical shift was set at 30.31 ppm by comparing the computed shift tensors with experimental chemical shielding values while maintaining the relative chemical shift differences. Out of at least 30 different structures generated for all the compositions, six distinct configurations of the 1:1 composition were selected to obtain the shift tensors. Their chemical shift values were then compared to the experimental data to obtain the model configuration. The dipolar coupling was also calculated with CASTEP by the method developed by Joyce et al. [71] using DFPT. The model structure was used to study the dipolar constant and the correlation between the amide and hydride ^1H in the solid solution. An open-source program, i.e., MagresView [72], was used to visualize the computed spectrum and NMR parameters. The structural models were visualized with Chemcraft 1.8.

3. Results

3.1. XRD analyses

The initial reactants, i.e., $CsNH_2$ and CsH, were first investigated using *ex-situ* XRD technique. The obtained and expected diffraction patterns are shown in Fig. 1. The diffraction peaks of the synthesized CsH are located at the same position as those of the standard CsH pattern (ICSD#53236). No additional peaks are detected. Similarly, the diffraction pattern of the synthesized $CsNH_2$ shows the typical peaks of the $CsNH_2$ phase in agreement with the standard $CsNH_2$ pattern (ICSD#25564). Also, in this case, no additional phases are observed. The cell structures at RT of CsH and $CsNH_2$ are cubic ($Fm\bar{3}m$) and tetragonal ($P4/nmm$), respectively.

The hand-ground mixtures of $CsNH_2$ and CsH in different stoichiometric ratios, i.e., x$CsNH_2$+(1-x)CsH, and x = {0, 0.1, 0.3, 0.5, 0.7, 0.9,

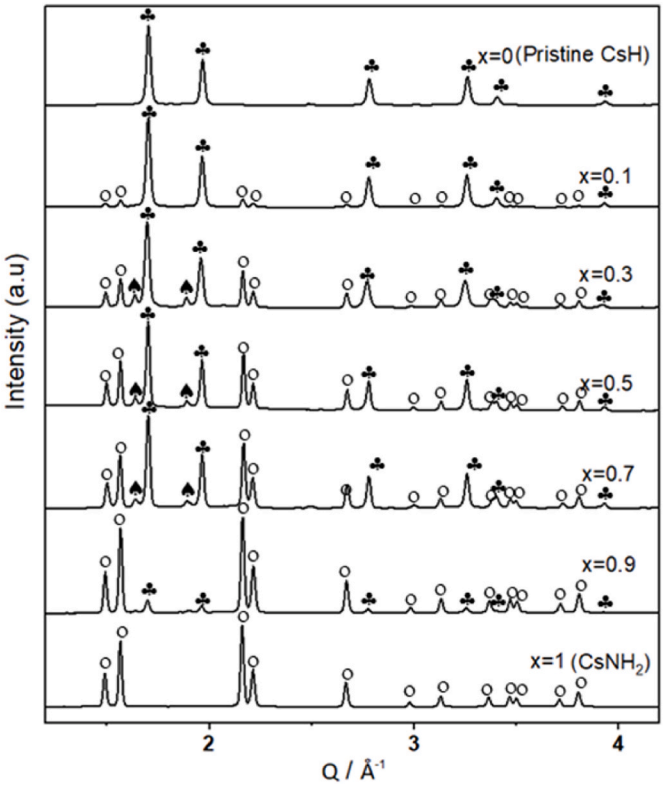

Fig. 2. Room temperature XRD diffractograms on x$CsNH_2$+(1-x)CsH collected after the hand-grinding. ♣ = CsH ($Fm\bar{3}m$), o = $CsNH_2$ ($P4/nmm$), ♠ = $CsNH_2$ ($Fm\bar{3}m$).

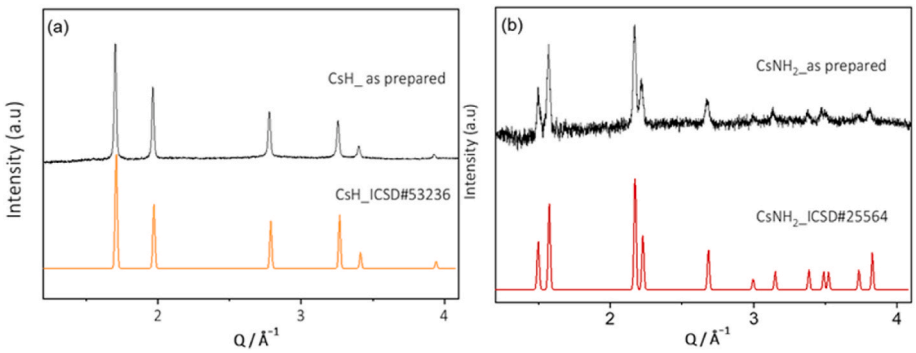

Fig. 1. Room temperature XRD patterns of synthesized CsH (a) and synthesized $CsNH_2$ samples (b). λ = 1.54184 Å.

1}, were characterized by *ex-situ* XRD and the results of this investigation are shown in Fig. 2. It can be seen that the diffraction peaks of the RT-structure of $CsNH_2$ (tetragonal, *s.g.* $P4/nmm$), and RT-structure of CsH (cubic, *s.g.* $Fm\bar{3}m$) are still observed for all investigated compositions. In addition, the diffraction peaks belonging to the high-temperature (HT) structure of $CsNH_2$ ($Fm\bar{3}m$) are identified for the compositions x = {0.3, 0.5, 0.7}.

In order to find out whether the conversion of the starting reactants into their solid solutions is possible, a part of the prepared mixtures of $CsNH_2$ and CsH was ball-milled and another part was thermally treated at 140 °C. The XRD diffractograms acquired at RT for the ball-milled and thermally treated samples are presented in Fig. 3a and b, respectively. As illustrated in Fig. 3a for the ball-milled samples, the tetragonal structure of $CsNH_2$ ($P4/nmm$) and cubic structure of CsH ($Fm\bar{3}m$) are not visible, but a newly developed cubic $Fm\bar{3}m$ structure, $Cs(NH_2)_xH_{1-x}$, is observed for the compositions with x = {0.1, 0.3, 0.5, 0.7}. Additionally, the presence of HT-modifications of $CsNH_2$, i.e., cubic structures $Pm\bar{3}m$, and $Fm\bar{3}m$, is detected for the samples with x = {0.1, 0.5}. In particular, the appearance of tetragonal $CsNH_2$ ($P4/nmm$) is noticed next to the new cubic $Cs(NH_2)_xH_{1-x}$ ($Fm\bar{3}m$) phase in the sample with x = 0.9, indicating either the disproportionation of the $Cs(NH_2)_xH_{1-x}$ solid solution or the incomplete reaction between the amide and the hydride phases. This point is discussed in more detail in the section related to the *in-situ* SR-PXD characterization. However, it is assumed that the mutual solubility of $CsNH_2$ and CsH leads to the formation of a new cubic structure $Cs(NH_2)_xH_{1-x}$, in all ball-milled samples. Due to the limited milling time, i.e., 10 min, only partial solubility is achieved. Moreover, it is clear at this point that the degree of inter-solubility strongly depends on the stoichiometric ratio of amide and hydride in the mixture. Similarly, XRD patterns at RT of mixed samples treated thermally were recorded, as shown in Fig. 3b. The data from this figure show that the reflections of the tetragonal $P4/nmm$ structure of $CsNH_2$ and cubic $Fm\bar{3}m$ structure of CsH are not detected, whereas the single cubic $Fm\bar{3}m$ phase $Cs(NH_2)_xH_{1-x}$ is observed for all compositions with x = {0.1, 0.3, 0.5, 0.7}, confirming the formation of the solid solution. For the samples with x = 0.9 prepared by ball-milling and by thermal treatment, the diffraction patterns show the presence of the tetragonal $CsNH_2$ ($P4/nmm$) and the cubic $Cs(NH_2)_xH_{1-x}$ ($Fm\bar{3}m$), thus indicating an incomplete conversion or instability of the solid solution for this composition. Comparing the results of the annealed samples with those of the ball-milled samples, it is evident that the temperature promotes the formation of the solid solution as it has already been reported in the literature for the potassium- and rubidium-based systems [11,46].

For the investigated systems, the phase formation and structural changes which occur during the heating and cooling process can be assessed by *in-situ* SR-PXD investigations. Fig. 4 presents the *in-situ* SR-PXD data collected for the ground $0.7CsNH_2$+0.3CsH composite. At the beginning of the heating period ($T \sim 26$ °C), it is possible to notice the reflections of the starting reactants, i.e., cubic CsH ($Fm\bar{3}m$) and tetragonal $CsNH_2$ ($P4/nmm$). Besides, diffraction peaks of the cubic $CsNH_2$ ($Fm\bar{3}m$) are also observed, indicating a partial phase transformation of $CsNH_2$ from tetragonal to cubic during hand-grinding. At $T \sim 35$ °C, the transition of the remaining tetragonal $CsNH_2$ to the cubic polymorph starts, in agreement with DTA observations (ESI-Fig. S2), and as was reported in Ref. [47]. With a further increase in temperature, the conversion of $CsNH_2$ from the tetragonal ($P4/nmm$) to the cubic polymorph is complete and another cubic $Fm\bar{3}m$ structure is also noticed, i.e., $Pm\bar{3}m$ at $T \sim 35$ °C and from $Pm\bar{3}m$ to $Fm\bar{3}m$ at $T \sim 55$ °C. These phase transformations are also visible in the *in-situ* SR-PXD pattern of the pristine $CsNH_2$ (Fig. 5), as discussed later. In addition, the diffraction peaks of CsH slightly shift to lower Q-values. The further increase of the temperature leads to the shift of the $CsNH_2$ ($Fm\bar{3}m$) reflections in the direction of higher Q-values and the CsH reflections toward lower Q-values. This process takes place until the diffraction peaks of these two phases merge to form a cubic ($Fm\bar{3}m$) solid solution, $Cs(NH_2)_xH_{1-x}$. At $T \sim 140$ °C (Fig. 4a and 4b), the transformation is nearly

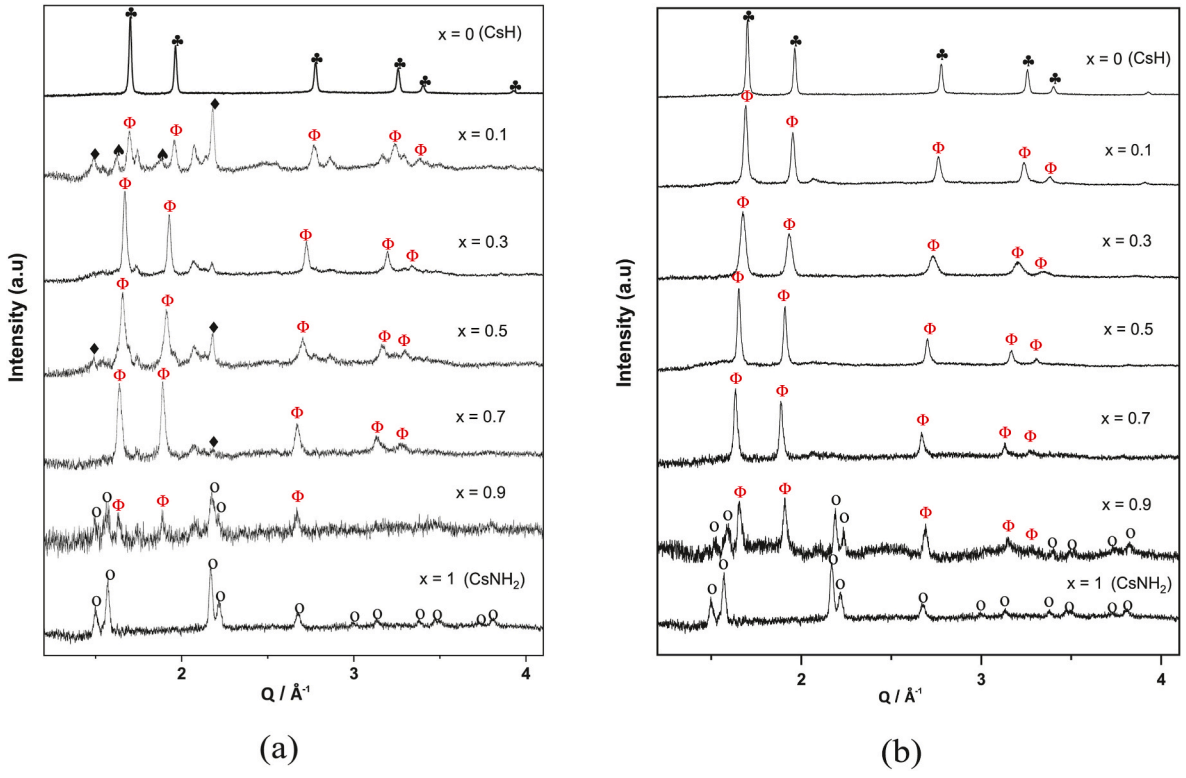

Fig. 3. Room temperature XRD diffractograms on $xCsNH_2$+(1-x)CsH collected after the ball milling (a) and after the heat treatment at 140 °C (b). ♣ = CsH ($Fm\bar{3}m$), o = $CsNH_2$ ($P4/nmm$), ◆ = $CsNH_2$ ($Pm\bar{3}m$), ♠ = $CsNH_2$ ($Fm\bar{3}m$), Φ = $Cs(NH_2)_xH_{1-x}$ ($Fm\bar{3}m$). λ = 1.54184 Å.

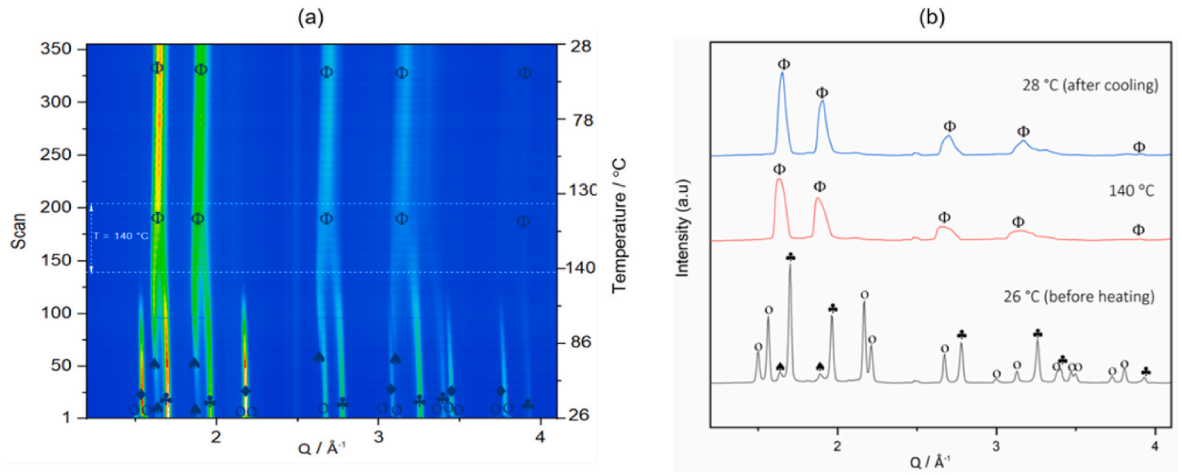

Fig. 4. *In-situ* SR-PXD measurement performed on the mixture 0.7$CsNH_2$+0.3CsH, at Petra III (P02.1), Desy (λ = 0.20761 Å). (a) Contour plot of *in-situ* SR-PXD and (b) Corresponding diffraction patterns collected at 26 °C, 140 °C, and 28 °C after cooling. ♣ = CsH (*Fm*$\bar{3}$*m*), o = $CsNH_2$ (*P*4/*nmm*), ◆ = $CsNH_2$ (*Pm*$\bar{3}$*m*), ♠ = $Cs(NH_2)$ (*Fm*$\bar{3}$*m*), Φ = $Cs(NH_2)_xH_{1-x}$ (*Fm*$\bar{3}$*m*).

finished and the growth of the single cubic solid solution $Cs(NH_2)_xH_{1-x}$ (*Fm*$\bar{3}$*m*) stops. During the cooling process, no phase changes are observed; however, the diffraction peaks of the $Cs(NH_2)_xH_{1-x}$ (*Fm*$\bar{3}$*m*), as expected, shift toward high Q-values due to the cell contraction. It should be noted that the XRD data of the heated sample shown in Figs. 3b and 4 do not match perfectly. This is most likely due to the different durations of the heat treatment for the two X-ray diffraction experiments (i.e., the investigated samples were kept isothermally for 3 h before acquiring *ex-situ* XRD in Fig. 3b, whereas this value is only 10 min in the *in-situ* SR-PXD experiments in Fig. 4).

In order to have a complete overview of the dependence of the solid solution formation on temperature and composition, the *in-situ* SR-PXD characterization of the samples x$CsNH_2$+(1-x)CsH with x = {0.1, 0.3, 0.5, 0.9}, plus the pristine reactants (CsH and $CsNH_2$) was also carried out and the results are displayed in Fig. 5. It can be seen that for the investigated temperature range, no phase transformations occur for the pristine CsH (x = 0), whereas for the pristine $CsNH_2$ (x = 1) the phase transformation from the tetragonal *P*4/*nmm* structure to the cubic *Pm*$\bar{3}$*m* structure takes place at a temperature around 35 °C and then *Pm*$\bar{3}$*m* to *Fm*$\bar{3}$*m* at about 55 °C, along with the intensity decrement of the cubic *Pm*$\bar{3}$*m*. During cooling, the HT cubic structure of $CsNH_2$ reverts to tetragonal geometry. In particular, similarly to the sample with x = 0.7, the partial phase transformation of $CsNH_2$ already started during the hand-grinding for the sample with x = {0.1, 0.3, 0.5}, while it is not observed for the other compositions with x = 0.9. As the temperature increases, for all investigated samples with x = {0.1, 0.3, 0.5, 0.9}, diffraction reflections of the $CsNH_2$ (*Fm*$\bar{3}$*m*) and the CsH (*Fm*$\bar{3}$*m*) shift towards each other to eventually form a new cubic *Fm*$\bar{3}$*m* phase $Cs(NH_2)_xH_{1-x}$, which is stable over the cooling step. At the end of *in-situ* SR-PXD experiments, clear differences in the X-ray diffraction patterns are noticed. For the samples with x = {0.1, 0.3, 0.5}, diffraction peaks of the cubic solid solution $Cs(NH_2)_xH_{1-x}$ (*Fm*$\bar{3}$*m*) are observed, suggesting the inter-solubility of $CsNH_2$ and CsH. On the contrary, for the sample with x = 0.9, the phase transformation of the cubic $CsNH_2$ to the tetragonal structure occurs at a temperature below 60 °C (during cooling), accompanying the presence of the solid solution $Cs(NH_2)_xH_{1-x}$ (*Fm*$\bar{3}$*m*). At the same time, no intensity decrement of the solid solution Cs $(NH_2)_xH_{1-x}$ (*Fm*$\bar{3}$*m*) is detected. This implies that the phase transition of $CsNH_2$ mentioned above for the sample with x = 0.9 is not related to the solid solution disproportionation, but to a lack of inter-solubility (at the investigated conditions). In other words, full solubility into the cubic phase cannot be attainable as the content of the amide phase is too high (≥0.9).

3.2. Experimental and simulated FT-IR analyses

The vibrational frequencies of the amide group of the pristine $CsNH_2$ and the annealed sample with x = 0.5 were characterized by the FT-IR technique and then compared with the theoretically calculated spectra (Fig. 6a and b, respectively). As seen in Fig. 6a, the stretching vibrational signals of the N–H bonds in $CsNH_2$ are observed at 3181 cm^{-1} and 3237 cm^{-1} while the N–H bending mode is detected at 1515 cm^{-1}. Similarly, the measured IR spectrum of the sample with x = 0.5 also shows the two stretching bands of the N–H bonds at wavenumbers of 3181 cm^{-1} and 3240 cm^{-1}, and the N–H bending vibrational band at 1515 cm^{-1}. The simulated IR spectra (Fig. 6b) show high-intensity modes for the $CsNH_2$, near 3261 cm^{-1} and 3340 cm^{-1} corresponding to the N–H stretching bands and at 1530 cm^{-1} for the N–H bending signal, whereas, for the x = 0.5 composition for which the solid solution structure of Cs $(NH_2)_{0.5}H_{0.5}$ was considered (ESI-Fig. S1), these two stretching signals at 3254 cm^{-1} and 3340 cm^{-1} and a bending mode at 1501 cm^{-1} were calculated. Comparing these results with the ones obtained experimentally, it is apparent that in both cases the strength of the bands of the x = 0.5 sample is weaker than those of pristine $CsNH_2$. Similar behavior is also observed for the other compositions with x = {0.2, 0.8} (ESI-Fig. S3), in which the strength of the vibrational modes is reduced corresponding to the reduction of amide content in the $Cs(NH_2)_xH_{1-x}$ mixtures. This is most likely due to the decrease of dipole moment caused by the reduction of negative charge on the nitrogen atom induced by the substituent (i.e., H), similar to the case of C–H bonds [73, 74]. The results of the infrared analysis show a good agreement between the simulated and the experimental data, especially for the main vibrational bands (ESI-Table S1), without applying a correction factor. A good agreement was obtained for the main stretching and bending vibrations, but the low frequencies were more difficult to match with the experimental data. It is also noticed that all the IR intensity calculations were made for periodic solid structures and the harmonic approximation was considered in the model structure for the IR vibrational calculations: this might lead to the remaining small discrepancies between the measured and the calculated vibrational spectra.

3.3. Experimental and simulated ^{1}H MAS NMR analyses

The formation of solid solutions under the interaction between $CsNH_2$ and CsH was further investigated by employing the ^{1}H MAS solid-state NMR technique along with computational NMR investigations. Fig. 7a shows the measured ^{1}H MAS NMR spectra of the starting materials and the x = 0.2, 0.5 and 0.8 samples. The chemical shift (*δ*) of amide

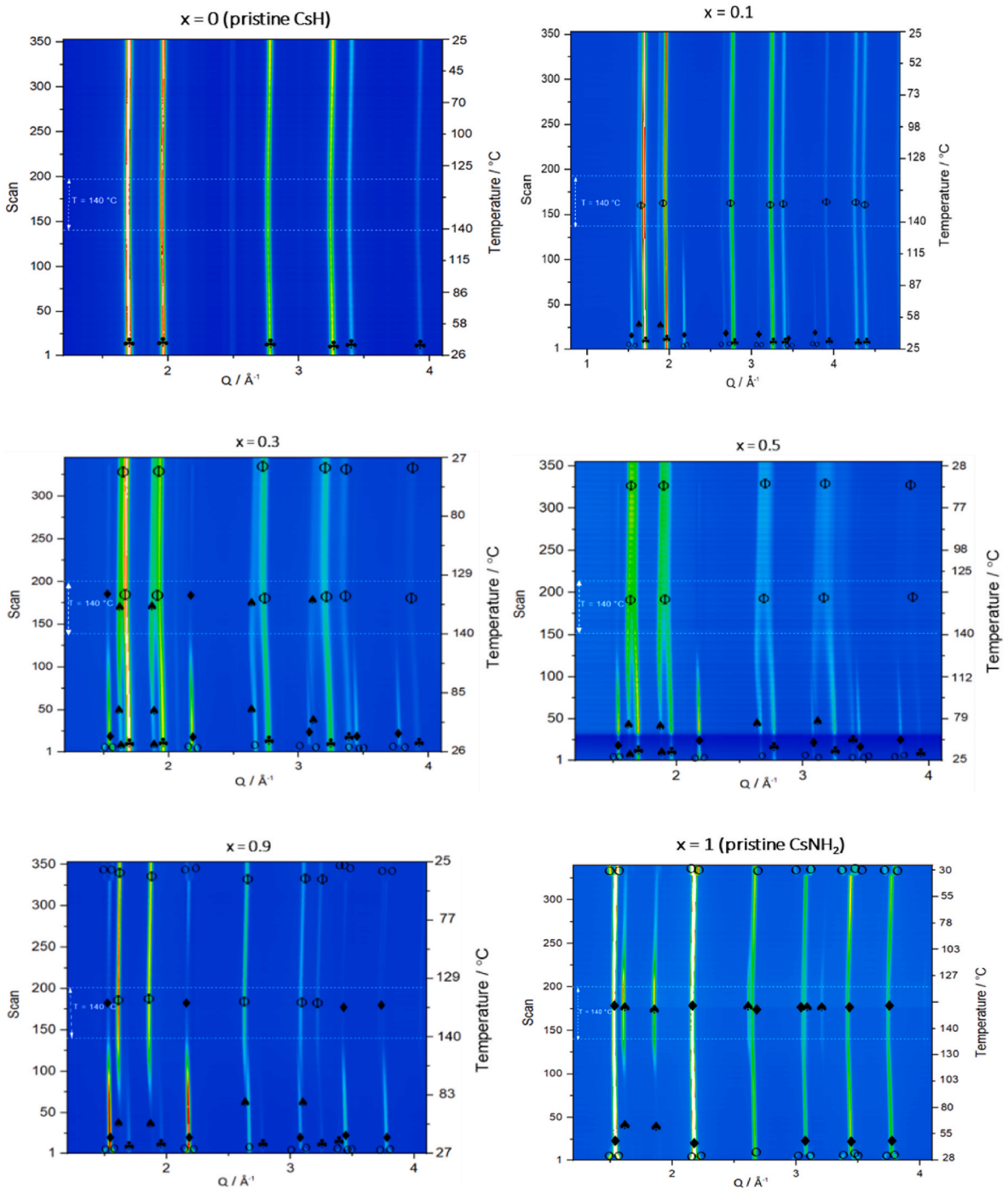

Fig. 5. *In-situ* SR-PXD measurement performed on $xCsNH_2$+(1-x)CsH samples, x = {0, 0.1, 0.3, 0.5, 0.9, 1}at Petra III, Desy (λ = 0.20761 Å). ♣ = CsH ($Fm\bar{3}m$), ○ = $CsNH_2$ ($P4/nmm$), ◆ = $CsNH_2$ ($Pm\bar{3}m$), ♠ = $Cs(NH_2)$ ($Fm\bar{3}m$), Φ = $Cs(NH_2)_xH_{1-x}$ ($Fm\bar{3}m$).

and hydride in the pure samples is found at −2.7 ppm and 8.8 ppm, respectively. For the x = 0.5 sample, the integrals of two signals flawlessly reflect the nominal relative amount of the solid solution, and no significant shift of the amide is observed, while the hydride signal slightly moves toward a higher frequency (δ = 9.9 ppm). In the simulated ^{1}H MAS NMR spectra (Fig. 7b), the chemical shifts (δ_{iso}, ppm) of hydride (H_a) and amide (H_b) are obtained at 8.0 ppm and −1.6 ppm, respectively. These signals are distinguishable in the $Cs(NH_2)_xH_{1-x}$ samples. The GIPAW calculated isotropic chemical shift (δ_{iso}, ppm) data for the hydride (H_a) and amide (H_b) ^{1}H in the $CsNH_2$, CsH, and Cs $(NH_2)_xH_{1-x}$ solid solutions are given in Table 1. Comparing these calculated values with those of the measured NMR data, it is obvious that the H_a and H_b peaks are distinct in the simulated NMR spectra, endorsing the assigned peak positions determined experimentally (Fig. 7 and Table 1) within a reasonable ~ 1–2 ppm chemical shift difference. This also validates the reliability of the selected model structure for comparison with the experimental studies.

3.4. 2D ^{1}H DQ MAS NMR analyses

The proximity between $CsNH_2$ and CsH is directly evaluated by the 2D ^{1}H DQ MAS NMR spectrum. Fig. 8 shows the 2D DQ experiment of

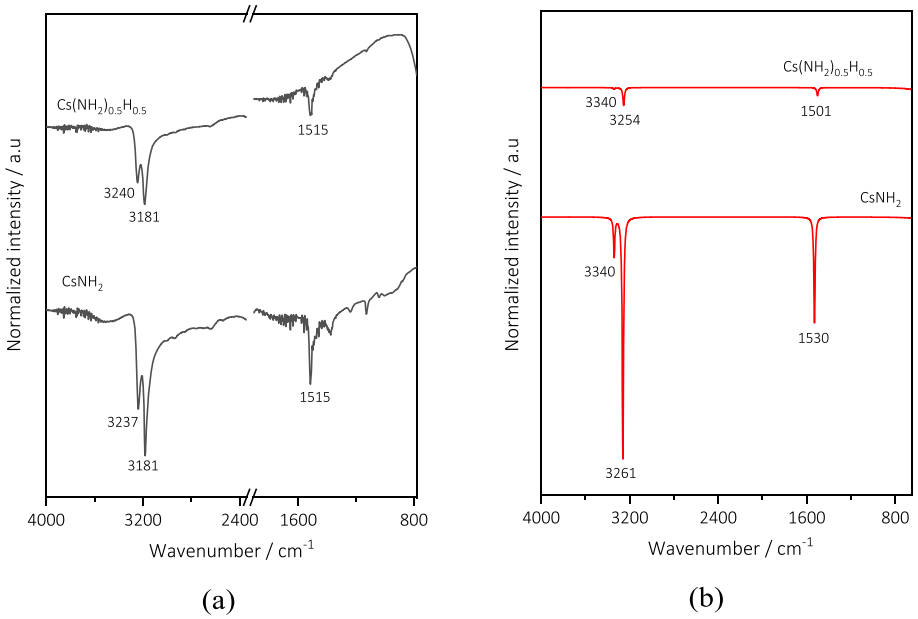

Fig. 6. (a) Experimental and (b) simulated IR spectra of the annealed $CsNH_2$ and $Cs(NH_2)_{0.5}H_{0.5}$.

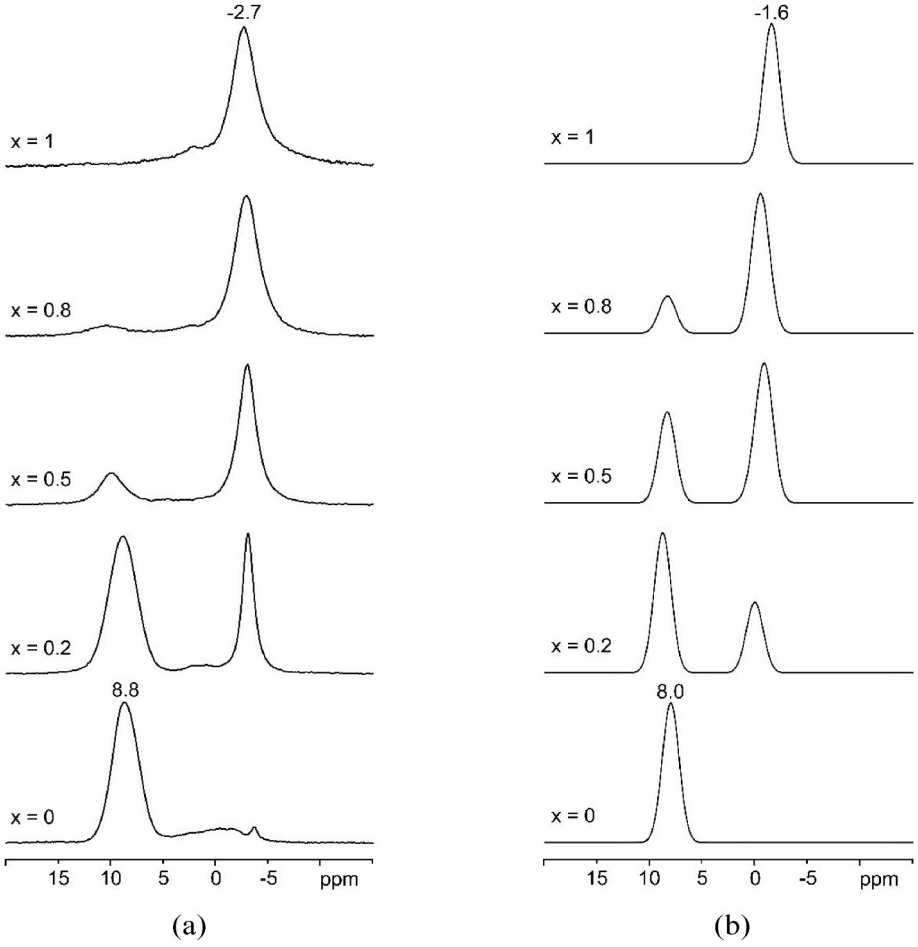

Fig. 7. (a) Experimental ^1H MAS NMR spectra of $xCsNH_2+(1-x)CsH$ samples and (b) corresponding simulated ^1H MAS NMR spectra of all compositions for which the solid solution structure of $Cs(NH_2)_xH_{1-x}$ was considered.

Table 1
Calculated and experimental ^{1}H SSNMR chemical shift of CsH, $CsNH_2$ and the Cs$(NH_2)_xH_{1-x}$.

System/Composition	Calculated ^{1}H δ_{iso} (ppm)	Experimental ^{1}H δ_{iso} (ppm)
$CsNH_2$	H_a: 1.6	−2.7
CsH	H_b: 8.0	8.8
$Cs(NH_2)_{0.2}H_{0.8}$	H_a: 0.0	−3.0
	H_b: 8.3	8.8
$Cs(NH_2)_{0.5}H_{0.5}$	H_a: 1.0	−3.1
	H_b: 8.4	9.9
$Cs(NH_2)_{0.8}H_{0.2}$	H_a: 0.8	−3.0
	H_b: 8.3	10.3

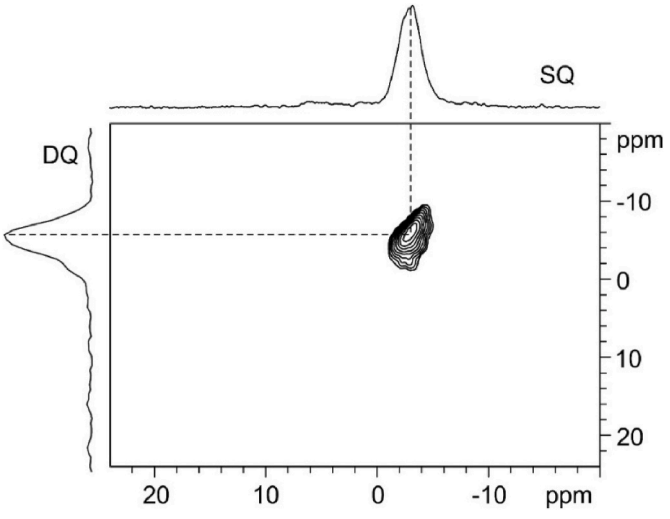

Fig. 8. 2D ^{1}H DQ MAS NMR spectrum of the $Cs(NH_2)_xH_{(1-x)}$sample, recorded at a spinning speed of 32 kHz.

the $Cs(NH_2)_{0.5}H_{0.5}$ sample, recorded at a spinning speed of 32 kHz. As presented in this figure, a single correlation that corresponds to an autopeak for the protons of $CsNH_2$ can be observed, while the autocorrelation signal for the protons of CsH is too weak to be seen in the ^{1}H DQ NMR spectrum. The latter signal, as well as any correlation peak between hydride and amide protons, was not observed either in the Cs$(NH_2)_{0.2}H_{0.8}$ sample or using a longer recoupling time (62.4 μs, equal to two rotor periods, instead of 31.2 μs, equal to one rotor period, commonly used for strong dipolar coupling). Two hypotheses related to the absence of H–H autopeaks and H–NH_2 correlations might be addressed: (i) the solid solution might not be well-achieved, or (ii) the unit cell of $Cs(NH_2)_{0.5}H_{0.5}$ is so large to strongly reduce, due to the $1/r^3$ dependence, the dipolar interaction between CsH and $CsNH_2$ or other CsH protons. In other words, the distance between CsH units and that between CsH and $CsNH_2$ units are larger than 3.5 Å [75–78]. Indeed, in the DQ experiments under fast MAS with spinning frequencies up to 35 kHz, the DQ coherences can usually be generated only between hydrogen atoms with interproton distances up to 3.5 Å [77,78].

4. Discussion

4.1. Anionic substitution and cell expansion

The XRD diffraction analyses reported in Figs. 3–5 indicate that the formation of a mixed cesium amide-hydride solid solution is possible over the whole compositional range and that the quantitative formation of a solid solution with a stable structure at RT is considerably influenced by the amide-hydride ratio. In this study, a complete conversion of the starting $CsNH_2$ and CsH into the $Cs(NH_2)_xH_{1-x}$ solid solution is only observed for the samples with x = {0.1, 0.3, 0.5, 0.7}. In addition, a clear shift of $Cs(NH_2)_xH_{1-x}$ diffraction peaks towards low Q-values with an increase of $CsNH_2$ content is noticed (see Fig. 3b), indicating the occurring ionic substitution of NH_2^-/H^- due to the different ionic radii between the NH_2^- (r_{ion} = 1.73 Å) and H^- (r_{ion} = 1.53 Å) anions. The formation of the cubic solid solution $Cs(NH_2)_xH_{1-x}$ ($Fm\bar{3}m$) suggests the full solubility of the two reacting species *via* the substitution of NH_2^- with H^- occurring upon heating. This is visible in the graph presented in Fig. 9, where the unit cell parameters of the cubic $Cs(NH_2)_xH_{1-x}$ solid solution (determined by Vegard's law and by the Rietveld refinement method) are plotted as the function of the amide molar fraction. Obviously, the unit cell of the solid solution is expanded with the increase of amide amount. This graph shows an excellent agreement between the cell parameters foreseen by Vegard's law and those obtained experimentally by Rietveld refinement.

4.2. Calculation of dipolar couplings

It is noticed that, as previously shown in Fig. 9, the obtained unit cell parameter of the $Cs(NH_2)_{0.5}H_{0.5}$ solid solution is as large as 6.560 Å, possibly due to the large size of elemental Cs (ionic radius r_{ion} = 181 p.m.), which reduced the dipolar couplings of distinct ^{1}H pairs in the solid solution. To examine these assumptions and to evaluate the experimental results regarding the formation of the solid solutions, the dipolar coupling, $R_{(DD)}$, between the protons of amide and hydride in the Cs$(NH_2)_{0.5}H_{0.5}$ solid solution was visualized with MagresView [72]. For comparison, the dipolar coupling was also computed for the homologous $Rb(NH_2)_{0.5}H_{0.5}$ solid solution for which the 2D ^{1}H DQ MAS NMR spectrum was previously reported [11]. As expected, the data presented in Table 2 show that the $R_{(DD)}$ values decrease as the distance between the protons, r, increases ($1/r^3$ dependence): despite being similar to the Rb system, the ^{1}H–^{1}H dipolar coupling is weaker in $Cs(NH_2)_{0.5}H_{0.5}$ due to the larger ^{1}H–^{1}H distance.

This can be better illustrated by showing the dipolar coupling between distinct H–H pairs on the respective models for the 1:1 composition of Cs and Rb solid solutions, as shown in Fig. 10. This figure shows that the closest interproton distance is 3.67 Å, with the respective dipolar coupling of ~2.44 kHz in the Cs system. At the same time, this value is smaller in the Rb system, i.e., the shortest interproton distance is about 3.29 Å, corresponding to a dipolar interaction of ~3.38 kHz. This could be caused by the fact that the larger Cs^+ cations (r_{ion} = 181 p.m.) versus Rb^+ ions (r_{ion} = 166 p.m.) also increase the range of interproton distances. This provides a clear insight into why the ^{1}H–^{1}H correlation

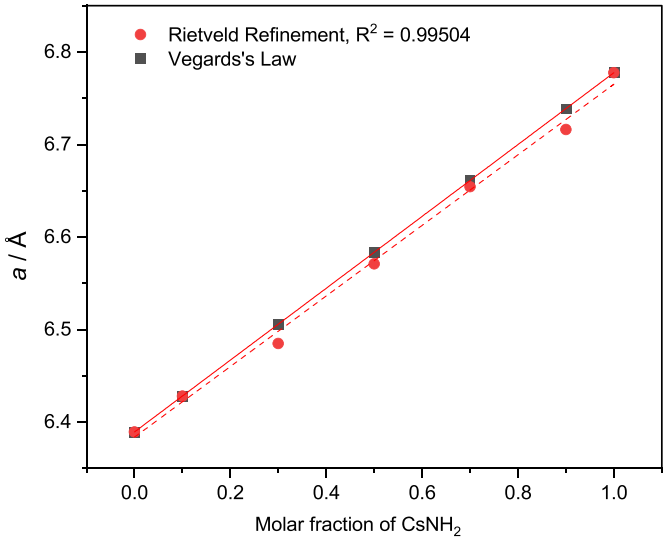

Fig. 9. Unit cell parameters of the $Cs(NH_2)_xH_{1-x}$ solid solution as a function of the amide fraction obtained from Rietveld refinement of the XRD data acquired after annealing and Vegard's law.

Table 2
Calculated dipolar coupling values in $Cs(NH_2)_{0.5}H_{0.5}$ and $Rb(NH_2)_{0.5}H_{0.5}$ together with the distances $r[H_a\text{-}H_b]$ between the respective protons.

System	$r[H_a - H_b]$ (Å)	$R_{(DD)}$ (kHz)
$Cs(NH_2)_{0.5}H_{0.5}$	3.66576	−2.44
	3.77645	−2.23
	3.81053	−2.17
	4.37055	−1.47
$Rb(NH_2)_{0.5}H_{0.5}$	3.22851	−3.57
	3.28928	−3.38
	4.52258	−1.30

peak between amide and hydride and hydride autocorrelation is not visible in the DQ experimental spectra (Fig. 9).

Verbraeken et al. [79] showed that BaH_2 exhibits hydride ionic conductivity rivaling that of the best-known proton conductors, which are generally considered the most promising ion conductors in the solid state. Rowberg et al. [80] demonstrated intensive studies on defect chemistry and ionic conduction in alkaline-earth hydrides (CaH_2, SrH_2, and BaH_2). The authors showed that ionic transport is mediated by hydrogen vacancies; their low formation energy and small migration barrier result in low overall activation energies for ionic conductivity. The extension of the high ionic conductivity of these metal hydrides can be obtained by doping impurities such as Na, K, Rb, and Cs. The Group 1 cations have only one valence electron compared to two for the alkaline-earth cations, and thus result in the reduced formation energy of hydrogen vacancies (V_H^+) and increased defect concentrations in the compound. For complex hydrides (*e.g.* amides, borohydrides, alanates), the partial ionic substitution, in which cations or anions in the solid-state lattice are partially replaced by other ions having a different ionic radius, is one of the common ways to improve the ionic conductivity of a material. The ionic substitution leads to the formation of either a double anion compound or a homogenous solid solution with different crystallographic structures, which affects the structural disorder of a material [81]. According to the observed results in this present work, it is also expected that the substitution of NH_2^-/H^- anionic species between amide and hydride could affect the disorder of structural lattices (or polarized anion sublattices) because of the different ionic sizes of $[NH_2]^-$ ($r_{ion} = 1.73$ Å) versus $[H]^-$ ($r_{ion} = 1.53$ Å), and subsequently change the functional properties of target materials (i.e., ionic conductivities), similar to the already known ionic conduction systems such as $LiBH_4$-LiX (X = Cl^-, Br^-, and I^-) [41,43] and $NaBH_4$–NaI [82]. Indeed, the lattice expansion associated with the dissolution of $[NH_2]^-$ into the CsH structure is observed, as shown in Fig. 9. Moreover, comparing the atomic radii of K, Rb, and Cs, their relative radii difference between them is less than 15%, which allows forming solid solutions according to Hume-Rothery rules. For these reasons, it is worth investigating the ionic conductivity of the alkali amide-hydride systems: MNH_2-MH (M = K, Rb, Cs) and their combinations. Further investigations on the ionic conduction of these mixed amide-hydride solid solutions within the compositional variation are ongoing in a following up research.

5. Conclusions

In this work, the formation of amide-hydride solid solutions for the $CsNH_2$–CsH system was thoroughly investigated by combining experimental determination and first-principles computational prediction. Within the scope of this study, the following results were obtained.

- A mixed cesium amide-hydride solid solution within the entire compositional range is formed *via* the NH_2^-/H^- anionic substitution.
- Full solubility into the cubic structure seems to be achievable, except when the content of the amide phase is too high ($x \geq 0.9$).
- The agreement between the experimental and computed data further reveals the further reveals the interaction of amide and hydride in their solid solution and confirms the formation of the solid solutions.

This work will be the base for further studies on the ionic conductivity of the mixed alkali amide-hydride solid solutions.

Credit author statement

Thi-Thu Le: Conceptualization, Methodology, Formal analysis, Investigation, Validation, Writing – original draft preparation, Archa Santhosh: Software, Resources, Formal analysis, Simone Bordignon: Resources, Investigation, Michele R. Chierotti: Resources, Investigation, Writing – review & editing, Paul Jerabek: Writing – review & editing, Thomas Klassen: Supervision, Funding acquisition, Claudio Pistidda: Conceptualization, Supervision, Writing – Review & Editting.

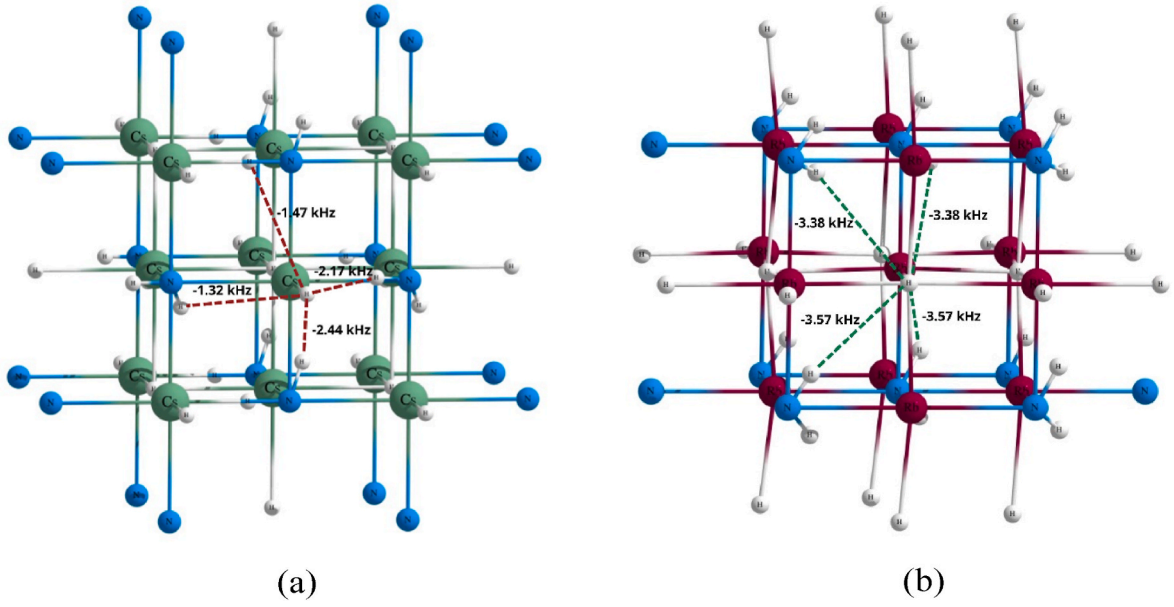

Fig. 10. Dipolar coupling constants between a selected ^1H in amide and ^1H in hydride, visualized for the model system of (a) $Cs(NH_2)_{0.5}H_{0.5}$ and (b) $Rb(NH_2)_{0.5}H_{0.5}$ systems. Green, purple, blue, and white corresponds to Cs, Rb, N, and H in the given order.

Declaration of competing interest

The authors declare that they have no known competing financial interests or personal relationships that could have appeared to influence the work reported in this paper.

Data availability

Data will be made available on request.

Acknowledgments

This research is funded by dtec. bw - Digitalization and Technology Research Center of Bundeswehr which we gratefully acknowledge.

Appendix A. Supplementary data

Supplementary data to this article can be found online at https://doi.org/10.1016/j.rineng.2023.100895.

References

[1] P. Chen, Z. Xiong, J. Luo, J. Lin, K.L. Tan, Interaction of hydrogen with metal nitrides and imides, Nature 420 (2002) 302–304.
[2] T. Ichikawa, K. Tokoyoda, H. Leng, H. Fujii, Hydrogen absorption properties of Li–Mg–N–H system, J. Alloys Compd. 400 (2005) 245–248.
[3] S. Orimo, Y. Nakamori, G. Kitahara, K. Miwa, N. Ohba, T. Noritake, S. Towata, Destabilization and enhanced dehydriding reaction of LiNH2: an electronic structure viewpoint, Appl. Phys. A 79 (2004) 1765–1767.
[4] W. Luo, E. Rönnebro, Towards a viable hydrogen storage system for transportation application, J. Alloys Compd. 404–406 (2005) 392–395.
[5] W. Luo, S. Sickafoose, Thermodynamic and structural characterization of the Mg–Li–N–H hydrogen storage system, J. Alloys Compd. 407 (2006) 274–281.
[6] Z. Xiong, J. Hu, G. Wu, P. Chen, W. Luo, K. Gross, J. Wang, Thermodynamic and kinetic investigations of the hydrogen storage in the Li–Mg–N–H system, J. Alloys Compd. 398 (2005) 235–239.
[7] N. Aslan, G. Gizer, C. Pistidda, M. Dornheim, M. Müller, S. Busch, W. Lohstroh, High hydrogen mobility in an amide–borohydride compound studied by quasielastic neutron scattering, Adv. Eng. Mater. 23 (2021), 2100620.
[8] G. Gizer, J. Puszkiel, H. Cao, C. Pistidda, T.T. Le, M. Dornheim, T. Klassen, Tuning the reaction mechanism and hydrogenation/dehydrogenation properties of 6Mg(NH2)29LiH system by adding LiBH4, Int. J. Hydrogen Energy 44 (2019) 11920–11929.
[9] G. Gizer, J. Puszkiel, M.V.C. Riglos, C. Pistidda, J.M. Ramallo-López, M. Mizrahi, A. Santoru, T. Gemming, J.-C. Tseng, T. Klassen, M. Dornheim, Improved kinetic behaviour of Mg(NH2)2-2LiH doped with nanostructured K-modified-LixTiyOz for hydrogen storage, Sci. Rep. 10 (2020) 8.
[10] A. Santoru, S. Garroni, C. Pistidda, C. Milanese, A. Girella, A. Marini, E. Masolo, A. Valentoni, N. Bergemann, T.T. Le, H. Cao, D. Haase, O. Balmes, K. Taube, G. Mulas, S. Enzo, T. Klassen, M. Dornheim, A new potassium-based intermediate and its role in the desorption properties of the K–Mg–N–H system, Phys. Chem. Chem. Phys. 18 (2016) 3910–3920.
[11] A. Santoru, C. Pistidda, M. Brighi, M.R. Chierotti, M. Heere, F. Karimi, H. Cao, G. Capurso, A.-L. Chaudhary, G. Gizer, S. Garroni, M.H. Sørby, B.C. Hauback, R. Černý, T. Klassen, M. Dornheim, Insights into the Rb–Mg–N–H system: an ordered mixed amide/imide phase and a disordered amide/hydride solid solution, Inorg. Chem. 57 (2018) 3197–3205.
[12] T. Ichikawa, S. Isobe, N. Hanada, H. Fujii, Lithium nitride for reversible hydrogen storage, J. Alloys Compd. 365 (2004) 271–276.
[13] P. Chen, Z. Xiong, J. Luo, J. Lin, K.L. Tan, Interaction between lithium amide and lithium hydride, J. Phys. Chem. B 107 (2003) 10967–10970.
[14] Z. Xiong, G. Wu, J. Hu, P. Chen, Ternary imides for hydrogen storage, Adv. Mater. 16 (2004) 1522–1525.
[15] S. Hino, T. Ichikawa, N. Ogita, M. Udagawa, H. Fujii, Quantitative estimation of NH3 partial pressure in H2 desorbed from the Li–N–H system by Raman spectroscopy, Chem. Commun. (2005) 3038–3040.
[16] J.W. Makepeace, J.M. Brittain, A. Sukhwani Manghnani, C.A. Murray, T.J. Wood, W.I.F. David, Compositional flexibility in Li–N–H materials: implications for ammonia catalysis and hydrogen storage, Phys. Chem. Chem. Phys. 23 (2021) 15091–15100.
[17] S. Garroni, A. Santoru, H. Cao, M. Dornheim, T. Klassen, C. Milanese, F. Gennari, C. Pistidda, Recent progress and new perspectives on metal amide and imide systems for solid-state hydrogen storage, Energies 11 (2018).
[18] H. Cao, Y. Zhang, J. Wang, Z. Xiong, G. Wu, P. Chen, Materials design and modification on amide-based composites for hydrogen storage, Prog. Nat. Sci.: Mater. Int. 22 (2012) 550–560.
[19] W. Luo, J. Wang, K. Stewart, M. Clift, K. Gross, Li–Mg–N–H: recent investigations and development, J. Alloys Compd. 446–447 (2007) 336–341.
[20] J. Wang, P. Chen, H. Pan, Z. Xiong, M. Gao, G. Wu, C. Liang, C. Li, B. Li, J. Wang, Solid–solid heterogeneous catalysis: the role of potassium in promoting the dehydrogenation of the Mg(NH2)2/2 LiH composite, ChemSusChem 6 (2013) 2181–2189.
[21] H.-J. Lin, H.-W. Li, H. Murakami, E. Akiba, Remarkably improved hydrogen storage properties of LiNH2-LiH composite via the addition of CeF4, J. Alloys Compd. 735 (2018) 1017–1022.
[22] G. Gizer, H. Cao, J. Puszkiel, C. Pistidda, A. Santoru, W. Zhang, T. He, P. Chen, T. Klassen, M. Dornheim, Enhancement effect of bimetallic amide K2Mn(NH2)4 and in-situ formed KH and Mn4N on the dehydrogenation/hydrogenation properties of Li–Mg–N–H system, Energies 12 (2019).
[23] C. Liang, Y. Liu, Z. Wei, Y. Jiang, F. Wu, M. Gao, H. Pan, Enhanced dehydrogenation/hydrogenation kinetics of the Mg(NH2)2–2LiH system with NaOH additive, Int. J. Hydrogen Energy 36 (2011) 2137–2144.
[24] H. Leng, X. Zhou, Y. Shi, J. Wei, Q. Li, K.-C. Chou, Improved hydrogen desorption properties of Li-N-H system by the combination of the catalytic effect of LiBH4 and microwave irradiation, Catal. Today 318 (2018) 91–96.
[25] G. Amica, P. Arneodo Larochette, F.C. Gennari, Hydrogen storage properties of LiNH2–LiH system with MgH2, CaH2 and TiH2 added, Int. J. Hydrogen Energy 40 (2015) 9335–9346.
[26] F. Torre, A. Valentoni, C. Milanese, C. Pistidda, A. Marini, M. Dornheim, S. Enzo, G. Mulas, S. Garroni, Kinetic improvement on the CaH2-catalyzed Mg(NH2)2+2LiH system, J. Alloys Compd. 645 (2015) S284–S287.
[27] L.L. Shaw, R. Ren, T. Markmaitree, W. Osborn, Effects of mechanical activation on dehydrogenation of the lithium amide and lithium hydride system, J. Alloys Compd. 448 (2008) 263–271.
[28] M. Matsumoto, T. Haga, Y. Kawai, Y. Kojima, Hydrogen desorption reactions of Li–N–H hydrogen storage system: estimation of activation free energy, J. Alloys Compd. 439 (2007) 358–362.
[29] Y. Liu, K. Zhong, K. Luo, M. Gao, H. Pan, Q. Wang, Size-dependent kinetic enhancement in hydrogen absorption and desorption of the Li−Mg−N−H system, J. Am. Chem. Soc. 131 (2009) 1862–1870.
[30] S. Isobe, T. Ichikawa, N. Hanada, H.Y. Leng, M. Fichtner, O. Fuhr, H. Fujii, Effect of Ti catalyst with different chemical form on Li–N–H hydrogen storage properties, J. Alloys Compd. 404–406 (2005) 439–442.
[31] H.Y. Leng, T. Ichikawa, S. Isobe, S. Hino, N. Hanada, H. Fujii, Desorption behaviours from metal–N–H systems synthesized by ball milling, J. Alloys Compd. 404–406 (2005) 443–447.
[32] T. Ichikawa, N. Hanada, S. Isobe, H.Y. Leng, H. Fujii, Hydrogen storage properties in Ti catalyzed Li–N–H system, J. Alloys Compd. 404–406 (2005) 435–438.
[33] C. Li, Y. Liu, Y. Gu, M. Gao, H. Pan, Improved hydrogen-storage thermodynamics and kinetics for an RbF-doped Mg(NH2)2–2 LiH system, Chem. Asian J. 8 (2013) 2136–2143.
[34] E. Napolitano, F. Dolci, R. Campesi, C. Pistidda, M. Hoelzel, P. Moretto, S. Enzo, Crystal structure solution of KMg(ND)(ND2): an ordered mixed amide/imide compound, Int. J. Hydrogen Energy 39 (2014) 868–876.
[35] J. Wang, G. Wu, Y.S. Chua, J. Guo, Z. Xiong, Y. Zhang, M. Gao, H. Pan, P. Chen, Hydrogen sorption from the Mg(NH2)2-KH system and synthesis of an amide–imide complex of KMg(NH)(NH2), ChemSusChem 4 (2011) 1622–1628.
[36] J. Zhang, Y. Liu, X. Zhang, Y. Yang, Q. Zhang, T. Jin, Y. Wang, M. Gao, L. Sun, H. Pan, Synthesis of CsH and its effect on the hydrogen storage properties of the Mg(NH2)2-2LiH system, Int. J. Hydrogen Energy 41 (2016) 11264–11274.
[37] J. Zhang, Y. Wang, M. Zhang, Z. Leng, M. Gao, J. Hu, Y. Liu, H. Pan, Improved overall hydrogen storage properties of a CsH and KH co-doped Mg(NH2)2/2LiH system by forming mixed amides of Li–K and Cs–Mg, RSC Adv. 7 (2017) 30357–30364.
[38] T. Durojaiye, J. Hayes, A. Goudy, Potassium, rubidium and cesium hydrides as dehydrogenation catalysts for the lithium amide/magnesium hydride system, Int. J. Hydrogen Energy 40 (2015) 2266–2273.
[39] P.E. de Jongh, D. Blanchard, M. Matsuo, T.J. Udovic, S. Orimo, Complex hydrides as room-temperature solid electrolytes for rechargeable batteries, Appl. Phys. A 122 (2016) 251.
[40] A. Unemoto, M. Matsuo, S.-i. Orimo, Complex hydrides for electrochemical energy storage, Adv. Funct. Mater. 24 (2014) 2267–2279.
[41] H. Maekawa, M. Matsuo, H. Takamura, M. Ando, Y. Noda, T. Karahashi, S.-i. Orimo, Halide-stabilized LiBH4, a room-temperature lithium fast-ion conductor, J. Am. Chem. Soc. 131 (2009) 894–895.
[42] M. Matsuo, A. Remhof, P. Martelli, R. Caputo, M. Ernst, Y. Miura, T. Sato, H. Oguchi, H. Maekawa, H. Takamura, A. Borgschulte, A. Züttel, S.-i. Orimo, Complex hydrides with (BH4)− and (NH2)− anions as new lithium fast-ion conductors, J. Am. Chem. Soc. 131 (2009) 16389–16391.
[43] M. Matsuo, H. Takamura, H. Maekawa, H.-W. Li, S.-i. Orimo, Stabilization of lithium superionic conduction phase and enhancement of conductivity of LiBH4 by LiCl addition, Appl. Phys. Lett. 94 (2009), 084103.
[44] W.I.F. David, M.O. Jones, D.H. Gregory, C.M. Jewell, S.R. Johnson, A. Walton, P. P. Edwards, A mechanism for non-stoichiometry in the lithium amide/lithium imide hydrogen storage reaction, J. Am. Chem. Soc. 129 (2007) 1594–1601.
[45] J.W. Makepeace, M.O. Jones, S.K. Callear, P.P. Edwards, W.I.F. David, In situ X-ray powder diffraction studies of hydrogen storage and release in the Li–N–H system, Phys. Chem. Chem. Phys. 16 (2014) 4061–4070.
[46] A. Santoru, C. Pistidda, M.H. Sørby, M.R. Chierotti, S. Garroni, E. Pinatel, F. Karimi, H. Cao, N. Bergemann, T.T. Le, J. Puszkiel, R. Gobetto, M. Baricco, B. C. Hauback, T. Klassen, M. Dornheim, KNH2–KH: a metal amide–hydride solid solution, Chem. Commun. 52 (2016) 11760–11763.
[47] R. Juza, A. Mehne, Zur kristallstruktur der Alkalimetallamide, Z. Anorg. Allg. Chem. 299 (1959) 33–40.

[48] R. Juza, H. Jacobs, W. Klose, Die Kristallstrukturen der Tieftemperaturmodifikationen von Kalium- und Rubidiumamid, Z. Anorg. Allg. Chem. 338 (1965) 171–178.
[49] J. Hayes, A. Goudy, Thermodynamics, kinetics and modeling studies of KH- RbH- and CsH-doped 2LiNH2/MgH2 hydrogen storage systems, Int. J. Hydrogen Energy 40 (2015) 12336–12342.
[50] R.V. Martins, N. Schell, T. Lippmann, F. Beckmann, H.-U. Ruhnau, R. Kiehn, A. Schreyer, The status of GKSS' high energy materials science beamline at Petra III, Acta Crystallogr. A 63 (2007) s246.
[51] U. Bösenberg, C. Pistidda, M. Tolkiehn, N. Busch, I. Saldan, K. Suarez-Alcantara, A. Arendarska, T. Klassen, M. Dornheim, Characterization of metal hydrides by in-situ XRD, Int. J. Hydrogen Energy 39 (2014) 9899–9903.
[52] C. Pistidda, A. Santoru, S. Garroni, N. Bergemann, A. Rzeszutek, C. Horstmann, D. Thomas, T. Klassen, M. Dornheim, First direct study of the ammonolysis reaction in the most common alkaline and alkaline earth metal hydrides by in situ SR-PXD, J. Phys. Chem. C 119 (2015) 934–943.
[53] L. Lutterotti, S. Matthies, H.R. Wenk, A.S. Schultz, J.W. Richardson, Combined texture and structure analysis of deformed limestone from time-of-flight neutron diffraction spectra, J. Appl. Phys. 81 (1997) 594–600.
[54] S.P. Ong, W.D. Richards, A. Jain, G. Hautier, M. Kocher, S. Cholia, D. Gunter, V. L. Chevrier, K.A. Persson, G. Ceder, Python Materials Genomics (pymatgen): a robust, open-source python library for materials analysis, Comput. Mater. Sci. 68 (2013) 314–319.
[55] G. Kresse, J. Furthmüller, Efficiency of ab-initio total energy calculations for metals and semiconductors using a plane-wave basis set, Comput. Mater. Sci. 6 (1996) 15–50.
[56] G. Kresse, J. Furthmüller, Efficient iterative schemes for ab initio total-energy calculations using a plane-wave basis set, Phys. Rev. B 54 (1996) 11169–11186.
[57] P.E. Blöchl, Projector augmented-wave method, Phys. Rev. B 50 (1994) 17953–17979.
[58] G. Kresse, D. Joubert, From ultrasoft pseudopotentials to the projector augmented-wave method, Phys. Rev. B 59 (1999) 1758–1775.
[59] J.P. Perdew, A. Ruzsinszky, G.I. Csonka, O.A. Vydrov, G.E. Scuseria, L. A. Constantin, X. Zhou, K. Burke, Restoring the density-gradient expansion for exchange in solids and surfaces, Phys. Rev. Lett. 100 (2008), 136406.
[60] S. Grimme, J. Antony, S. Ehrlich, H. Krieg, A consistent and accurate ab initio parametrization of density functional dispersion correction (DFT-D) for the 94 elements H-Pu, J. Chem. Phys. 132 (2010), 154104.
[61] S. Grimme, S. Ehrlich, L. Goerigk, Effect of the damping function in dispersion corrected density functional theory, J. Comput. Chem. 32 (2011) 1456–1465.
[62] S. Baroni, S. de Gironcoli, A. Dal Corso, P. Giannozzi, Phonons and related crystal properties from density-functional perturbation theory, Rev. Mod. Phys. 73 (2001) 515–562.
[63] K. Refson, P.R. Tulip, S.J. Clark, Variational density-functional perturbation theory for dielectrics and lattice dynamics, Phys. Rev. B 73 (2006), 155114.
[64] A. Togo, I. Tanaka, First principles phonon calculations in materials science, Scripta Mater. 108 (2015) 1–5.
[65] J.M. Skelton, L.A. Burton, A.J. Jackson, F. Oba, S.C. Parker, A. Walsh, Lattice dynamics of the tin sulphides SnS2, SnS and Sn2S3: vibrational spectra and thermal transport, Phys. Chem. Chem. Phys. 19 (2017) 12452–12465.
[66] C.J. Pickard, F. Mauri, All-electron magnetic response with pseudopotentials: NMR chemical shifts, Phys. Rev. B 63 (2001), 245101.
[67] S.J. Clark, M.D. Segall, C.J. Pickard, P.J. Hasnip, M.I.J. Probert, K. Refson, M. C. Payne, First principles methods using CASTEP, Z. für Kristallogr. - Cryst. Mater. 220 (2005) 567–570.
[68] J.R. Yates, C.J. Pickard, F. Mauri, Calculation of NMR chemical shifts for extended systems using ultrasoft pseudopotentials, Phys. Rev. B 76 (2007), 024401.
[69] S.K. Wolff, T. Ziegler, E. van Lenthe, E.J. Baerends, Density functional calculations of nuclear magnetic shieldings using the zeroth-order regular approximation (ZORA) for relativistic effects: ZORA nuclear magnetic resonance, J. Chem. Phys. 110 (1999) 7689–7698.
[70] A. Tkatchenko, M. Scheffler, Accurate molecular van der waals interactions from ground-state electron density and free-atom reference data, Phys. Rev. Lett. 102 (2009), 073005.
[71] S.A. Joyce, J.R. Yates, C.J. Pickard, F. Mauri, A first principles theory of nuclear magnetic resonance J-coupling in solid-state systems, J. Chem. Phys. 127 (2007), 204107.
[72] S. Sturniolo, T.F.G. Green, R.M. Hanson, M. Zilka, K. Refson, P. Hodgkinson, S. P. Brown, J.R. Yates, Visualization and processing of computed solid-state NMR parameters: MagresView and MagresPython, Solid State Nucl. Magn. Reson. 78 (2016) 64–70.
[73] M. Cinar, A. Coruh, M. Karabacak, I.R. Ft, UV–vis, 1H and 13C NMR spectra and the equilibrium structure of organic dye molecule disperse red 1 acrylate: a combined experimental and theoretical analysis, Spectrochim. Acta Mol. Biomol. Spectrosc. 83 (2011) 561–569.
[74] H. Spedding, D.H. Whiffen, Intensities in the infra-red spectrum of benzene, Proc. Roy. Soc. Lond. Math. Phys. Sci. 238 (1956) 245–255.
[75] T. Kobayashi, K. Mao, P. Paluch, A. Nowak-Król, J. Sniechowska, Y. Nishiyama, D. T. Gryko, M.J. Potrzebowski, M. Pruski, Study of intermolecular interactions in the corrole matrix by solid-state NMR under 100 kHz MAS and theoretical calculations, Angew. Chem. Int. Ed. 52 (2013) 14108–14111.
[76] S.P. Brown, Probing proton–proton proximities in the solid state, Prog. Nucl. Magn. Reson. Spectrosc. 50 (2007) 199–251.
[77] J.M. Griffin, D.R. Martin, S.P. Brown, Distinguishing anhydrous and hydrous forms of an active pharmaceutical ingredient in a tablet formulation using solid-state NMR spectroscopy, Angew. Chem. Int. Ed. 46 (2007) 8036–8038.
[78] I. Schnell, H.W. Spiess, High-resolution 1H NMR spectroscopy in the solid state: very fast sample rotation and multiple-quantum coherences, J. Magn. Reson. 151 (2001) 153–227.
[79] M.C. Verbraeken, C. Cheung, E. Suard, J.T.S. Irvine, High H− ionic conductivity in barium hydride, Nat. Mater. 14 (2015) 95–100.
[80] A.J.E. Rowberg, L. Weston, C.G. Van de Walle, Ion-transport engineering of alkaline-earth hydrides for hydride electrolyte applications, Chem. Mater. 30 (2018) 5878–5885.
[81] M. Matsuo, H. Oguchi, T. Sato, H. Takamura, E. Tsuchida, T. Ikeshoji, S.-i. Orimo, Sodium and magnesium ionic conduction in complex hydrides, J. Alloys Compd. 580 (2013) S98–S101.
[82] M. Matsuo, S. Kuromoto, T. Sato, H. Oguchi, H. Takamura, S.-i. Orimo, Sodium ionic conduction in complex hydrides with [BH4]− and [NH2]− anions, Appl. Phys. Lett. 100 (2012), 203904.